FLOW TRANSITION WITH 2-D ROUGHNESS ELEMENTS IN A 3-D CHANNEL

Zhining Liu, Chaoqun Liu, and Stephen F. McCormick
Computational Mathematics Group, University of Colorado at Denver
Denver, CO

SUMMARY

We develop a new numerical approach to study the spatially evolving instability of the streamwise dominant flow in the presence of roughness elements. The difficulty in handling the flow over the boundary surface with general geometry is removed by using a new conservative form of the governing equations and an analytical mapping. The numerical scheme uses second-order backward Euler in time, fourth-order central differences in all three spatial directions, and boundary-fitted staggered grids. A three-dimensional channel with multiple two-dimensional-type roughness elements is employed as the test case. Fourier analysis is used to decompose different Fourier modes of the disturbance. The results show that surface roughness leads to transition at lower Reynolds number than for smooth channels.

INTRODUCTION

Transition from laminar to turbulent flow is a phenomenon of great importance and practical interest. Major experimental work in aerodynamics has been pursued to study boundary layer transition, and this in turn has led to a critical need for further understanding of this fundamental process. Unfortunately, to date, no reliable methods exist for predicting transition in the presence of surface roughness, either experimentally or numerically. In fact, there are many factors that affect transition, such as solid wall temperature, solid wall curvature, pressure gradients, free-stream disturbance, and surface roughness. There has been some experimental activity dealing with the effect of both 2-D and 3-D roughness elements on transition from laminar to turbulent flow. For example, Klebanoff et al showed that surface roughness induces early transition [1]. Also, others have obtained limited numerical results with 2-D flow [2].

The purpose of the present work is to develop new efficient and easy-to-use methods for numerical simulation of the effect of surface roughness on flow transition. A new conservative form of the governing equations is derived. Because of the high sensitivity of transitional flows, a high order scheme based on our earlier work (cf. [3] – [6]) is developed. For the grid generation scheme, an analytical map is used, so the Jacobian coefficients are computed exactly. Moreover, we develop the governing equation in a form that enables a much simpler numerical process.

We impose single and multiple 2-D-type roughness elements on the lower solid wall to test the effect of surface roughness on flow transition. A Fourier transformation is employed to analyze different modes of the resulting disturbance. The computational results show that the induced mean flow distortion and other high frequency waves make the flow more unstable.

* This work was supported by NASA under grant number NAS1-19312.

GOVERNING EQUATIONS

In this study, the three-dimensional, time-dependent, incompressible Navier-Stokes equations, which are nondimensionalized by the channel half-height h and the centerline velocity U_∞ are considered as the governing equations for 3-D channel flow (Figure 1):

$$\frac{\partial u}{\partial t}+\frac{\partial uu}{\partial x}+\frac{\partial uv}{\partial y}+\frac{\partial uw}{\partial z}-\frac{1}{Re}(\frac{\partial^2 u}{\partial x^2}+\frac{\partial^2 u}{\partial y^2}+\frac{\partial^2 u}{\partial z^2})+\frac{\partial P}{\partial x}=0, \tag{1}$$

$$\frac{\partial v}{\partial t}+\frac{\partial vu}{\partial x}+\frac{\partial vv}{\partial y}+\frac{\partial vw}{\partial z}-\frac{1}{Re}(\frac{\partial^2 v}{\partial x^2}+\frac{\partial^2 v}{\partial y^2}+\frac{\partial^2 v}{\partial z^2})+\frac{\partial P}{\partial y}=0, \tag{2}$$

$$\frac{\partial w}{\partial t}+\frac{\partial wu}{\partial x}+\frac{\partial wv}{\partial y}+\frac{\partial ww}{\partial z}-\frac{1}{Re}(\frac{\partial^2 w}{\partial x^2}+\frac{\partial^2 w}{\partial y^2}+\frac{\partial^2 w}{\partial z^2})+\frac{\partial P}{\partial z}=0, \tag{3}$$

$$\frac{\partial u}{\partial x}+\frac{\partial v}{\partial y}+\frac{\partial w}{\partial z}=0, \tag{4}$$

where u, v, and w are velocity components in the $x-$, $y-$, and $z-$ directions, respectively, P is the pressure, and Re is the Reynolds number based on the centerline velocity U_∞ of mean flow, the channel half-height h, and the viscosity parameter ν:

$$Re=\frac{U_\infty h}{\nu}. \tag{5}$$

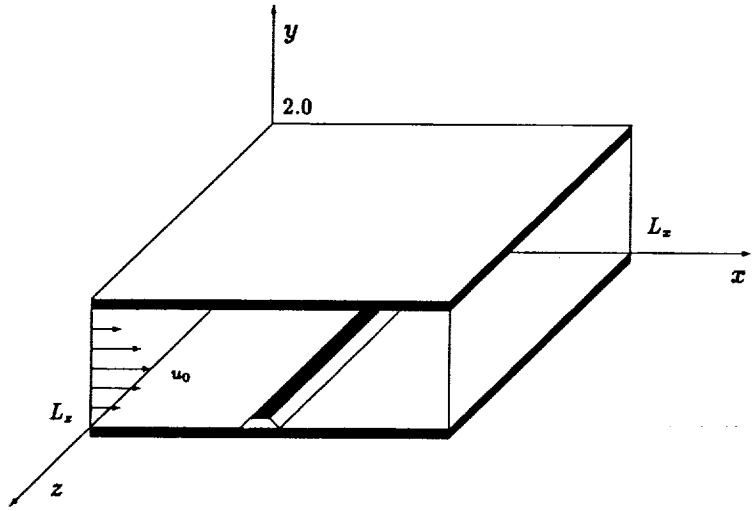

Figure 1. 3-D channel with a single 2-D-type roughness element.

For the current work, we consider a special mapping

$$\begin{array}{lll} x=\xi & & \xi=x \\ y=y(\xi,\eta,\zeta) & \text{or} & \eta=\eta(x,y,z) \\ z=\zeta & & \zeta=z, \end{array}$$

which implies that

$$\begin{aligned} J &= \eta_y, \\ \xi_x &= \zeta_z=1, \\ \xi_z &= \zeta_x=0, \end{aligned}$$

and the final forms of the momentum and continuity equations are:

$$\frac{\partial u}{\partial t}+\eta_y(\frac{\partial uU}{\partial \xi}+\frac{\partial uV}{\partial \eta}+\frac{\partial uW}{\partial \zeta})+(\frac{\partial}{\partial \xi}+\eta_x\frac{\partial}{\partial \eta})P-\frac{1}{Re}\Delta_1 u=0, \tag{6}$$

$$\frac{\partial v}{\partial t}+\eta_y(\frac{\partial vU}{\partial \xi}+\frac{\partial vV}{\partial \eta}+\frac{\partial vW}{\partial \zeta})+\eta_y\frac{\partial P}{\partial \eta}-\frac{1}{Re}\Delta_1 v=0, \tag{7}$$

$$\frac{\partial w}{\partial t}+\eta_y(\frac{\partial wU}{\partial \xi}+\frac{\partial wV}{\partial \eta}+\frac{\partial wW}{\partial \zeta})+(\eta_z\frac{\partial}{\partial \eta}+\frac{\partial}{\partial \zeta})P-\frac{1}{Re}\Delta_1 w=0, \tag{8}$$

$$\frac{\partial U}{\partial \xi}+\frac{\partial V}{\partial \eta}+\frac{\partial W}{\partial \zeta}=0, \tag{9}$$

for the total flow, or

$$\frac{\partial u}{\partial t}+\eta_y(\frac{\partial[u(U+U_0)+u_0U]}{\partial \xi}+\frac{\partial[u(V+V_0)+u_0V]}{\partial \eta}+\frac{\partial[u(W+W_0)+u_0W]}{\partial \zeta})$$
$$+(\frac{\partial}{\partial \xi}+\eta_x\frac{\partial}{\partial \eta})P-\frac{1}{Re}\Delta_1 u=0, \tag{10}$$

$$\frac{\partial v}{\partial t}+\eta_y(\frac{\partial[v(U+U_0)+v_0U]}{\partial \xi}+\frac{\partial[v(V+V_0)+v_0V]}{\partial \eta}+\frac{\partial[v(W+W_0)+v_0W]}{\partial \zeta})$$
$$+\eta_y\frac{\partial P}{\partial \eta}-\frac{1}{Re}\Delta_1 v=0, \tag{11}$$

$$\frac{\partial w}{\partial t}+\eta_y(\frac{\partial[w(U+U_0)+w_0U]}{\partial \xi}+\frac{\partial[w(V+V_0)+w_0V]}{\partial \eta}+\frac{\partial[w(W+W_0)+w_0W]}{\partial \zeta})$$
$$+(\eta_z\frac{\partial}{\partial \eta}+\frac{\partial}{\partial \zeta})P-\frac{1}{Re}\Delta_1 w=0, \tag{12}$$

$$\frac{\partial U}{\partial \xi}+\frac{\partial V}{\partial \eta}+\frac{\partial W}{\partial \zeta}=0, \tag{13}$$

for the perturbation flow, where,

$$\Delta_1=\frac{\partial^2}{\partial \xi^2}+(\eta_x^2+\eta_y^2+\eta_z^2)\frac{\partial^2}{\partial \eta^2}+\frac{\partial^2}{\partial \zeta^2}+2\eta_x\frac{\partial^2}{\partial \xi\partial \eta}+2\eta_z\frac{\partial^2}{\partial \eta\partial \zeta}+(\eta_{xx}+\eta_{yy}+\eta_{zz})\frac{\partial}{\partial \eta}. \tag{14}$$

The inverse transformation of the variables under this special mapping becomes

$$u = U\eta_y, \tag{15}$$
$$w = W\eta_y, \tag{16}$$
$$v = V-U\eta_x-W\eta_z. \tag{17}$$

Here we have seven unknowns (u, v, w, P, U, V, W), seven equations ((6) – (9), (15) – (17)) for the base flow or total flow, and seven equations ((10)–(13), (15) – (17)) for the perturbation.

Our solution process is outlined as follows:

1. Perform the surface and grid generation process to obtain the required Jacobian coefficients.

2. Solve system (6) – (9) and (15) – (17) to obtain the base flow solution.

3. Solve system (10)–(13) and (15) – (17) to obtain the perturbation solution based on the above base flow.

For the channel flow, though the boundary conditions are quite simple, there are still some difficulties we need to overcome. The so-called buffer domain [7] technique is used here for both the base flow and perturbation. For details, see [6]. The boundary condition for the solid wall is the no-slip boundary condition:

$$u_{wall} = v_{wall} = w_{wall} = U_{wall} = V_{wall} = W_{wall} = 0. \tag{18}$$

No boundary condition is needed for the pressure at the solid wall since we use a staggered grid. For the inflow, Poiseuille flow is imposed at the inlet for the base flow solution, and the eigenfunctions obtained from the linear stability theory with specified Reynolds number are employed at the flow inlet for the perturbation. The final outflow boundary conditions are:

- for the base flow,

$$\begin{aligned} \frac{\partial^2 U}{\partial \xi^2} &= 0 \quad \text{for } U, \\ \frac{\partial^2 V}{\partial \xi^2} &= 0 \quad \text{for } V, \\ \frac{\partial^2 W}{\partial \xi^2} &= 0 \quad \text{for } W, \end{aligned} \tag{19}$$

- for the perturbation flow,

$$\begin{aligned} \frac{\partial U}{\partial \xi} + \frac{\partial V}{\partial \eta} + \frac{\partial W}{\partial \zeta} &= 0 \quad \text{for } U, \\ \frac{\partial^2 V}{\partial \xi^2} &= 0 \quad \text{for } V, \\ \frac{\partial^2 W}{\partial \xi^2} &= 0 \quad \text{for } W, \end{aligned} \tag{20}$$

and the associated u, v, w can similarly be obtained by the inverse transformation (15) – (17).

Periodicity is assumed in the spanwise $\zeta-$direction.

NUMERICAL PROCEDURE

Surface and Grid Generation

Assume that no stagnation points exist in the computational domain. Solitary type roughness elements are overlapped on the lower solid wall of the channel to simulate surface roughness. For the 2-D roughness elements (because the grid is uniform and the domain is periodic in the spanwise z direction, we need only discuss the 2-D case here), the surface can be expressed as

$$f(x) = \sum_{l=1}^{m} \kappa_l sech^2(b_l(x - x_l)), \tag{21}$$

where κ_l is the height of the roughness element, b_l is a parameter for adjusting the curvature rate of the roughness element, and x_l is the peak point coordinate.

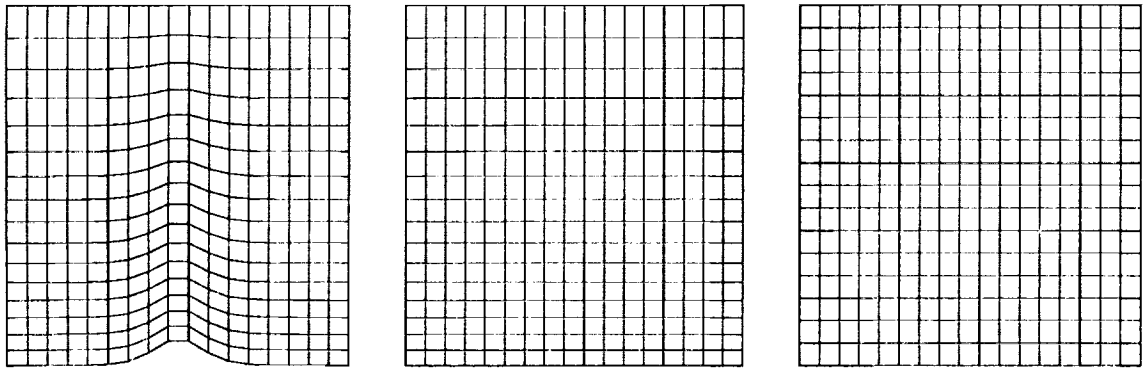

Figure 2. Physical, stretched, and uniform grids.

Our grid generation approach consists of two mappings(see Figure 2):

- from the physical grid that conforms to the rough boundary to the stretched intermediate grid that is uniform in the x direction but nonuniform in y,
- from the stretched grid to the uniform computational grid.

The resulting mapping from the physical to the uniform computational grid is

$$\eta = \frac{y_{max}(\sigma + y_{max})(y - f(x))}{y_{max}(\sigma + y) - f(x)(\sigma + y_{max})}, \tag{22}$$

and its inverse map is

$$y = \frac{\eta\sigma(y_{max} - f(x)) + y_{max}f(x)(\sigma + y_{max} - \eta)}{y_{max}(\sigma + y_{max} - \eta)}, \tag{23}$$

where y_{max} is the maximum height of the computational domain and σ is the parameter for adjusting the density of grids near the lower solid wall. The required Jacobian coefficients are

$$\eta_x = \frac{y_{max}f_x\sigma(\sigma + y_{max})(y - y_{max})}{[y_{max}(\sigma + y) - f(x)(\sigma + y_{max})]^2}, \tag{24}$$

$$\eta_y = \frac{y_{max}\sigma(\sigma + y_{max})(y_{max} - f(x))}{[y_{max}(\sigma + y) - f(x)(\sigma + y_{max})]^2}, \tag{25}$$

$$\eta_{xx} = y_{max}\sigma(\sigma + y_{max})(y - y_{max}) \frac{f_{xx}[y_{max}(\sigma + y) - f(x)(\sigma + y_{max})] + 2f_x^2(\sigma + y_{max})}{[y_{max}(\sigma + y) - f(x)(\sigma + y_{max})]^3}, \tag{26}$$

$$\eta_{yy} = \frac{-2y_{max}^2\sigma(\sigma + y_{max})(y_{max} - f(x))}{[y_{max}(\sigma + y) - f(x)(\sigma + y_{max})]^3}, \tag{27}$$

$$\eta_x = \eta_{zz} = 0. \tag{28}$$

Here, $f_x = \frac{\partial f}{\partial x}$ and $f_{xx} = \frac{\partial^2 f}{\partial x^2}$.

Discretization

In the computational $(\xi,\ \eta,\ \zeta)$ space, the grids are uniform. Suppose $u,\ v,\ w$ and $U,\ V,\ W$ are defined in terms of a staggered grid in the computational space (see Figure 3). Here, the values of P are associated with its cell centers, u and U with centers of the cell surfaces parallel to the (η,ζ) plane, v and V with centers of the cell surfaces parallel to the (ξ,ζ) plane, and w and W with centers of the cell surfaces parallel to the (ξ,η) plane.

Second-order backward Euler differences are used in the time direction, and fourth-order central differences are used in space. Details of such an approach can be found in [5]. With those assumptions, we can write the discretized governing equations symbolically as follows:

$$\begin{aligned}
A_{EE}u_{EE} + A_E u_E + A_W u_W + A_{WW}u_{WW} + A_{NN}u_{NN} + A_N u_N + A_S u_S + A_{SS}u_{SS} \; + \\
A_{FF}u_{FF} + A_F u_F + A_B u_B + A_{BB}u_{BB} - A_C u_C + D_{WW}P_{WW} + D_W P_W + D_E P_E - D_C P_C &= S_u, \quad (29)\\
B_{EE}v_{EE} + B_E v_E + B_W v_W + B_{WW}v_{WW} + B_{NN}v_{NN} + B_N v_N + B_S v_S + B_{SS}v_{SS} \; + \\
B_{FF}v_{FF} + B_F v_F + B_B v_B + B_{BB}v_{BB} - B_C v_C + E_{SS}P_{SS} + E_S P_S + E_N P_N - E_C P_C &= S_v, \quad (30)\\
C_{EE}w_{EE} + C_E w_E + C_W w_W + C_{WW}w_{WW} + C_{NN}w_{NN} + C_N w_N + C_S w_S + C_{SS}w_{SS} \; + \\
C_{FF}w_{FF} + C_F w_F + C_B w_B + C_{BB}w_{BB} - C_C w_C + F_{BB}P_{BB} + F_B P_B + F_F P_F - F_C P_C &= S_w, \quad (31)\\
DU_{EE}U_{EE} + DU_E U_E + DU_W U_W - DU_C U_C + DV_{NN}V_{NN} + DV_N V_N \; + \\
DV_S V_S - DV_C V_C + DW_{FF}W_{FF} + DW_F W_F + DW_B W_B - DW_C W_C &= S_m, \quad (32)
\end{aligned}$$

$$\begin{aligned}
u_C &= \eta_y^{uc} U_C, && (33)\\
w_C &= \eta_y^{wc} W_C, && (34)\\
v_C &= \eta_x^{vc} U_c + V_C + \eta_z^{vc} W_c. && (35)
\end{aligned}$$

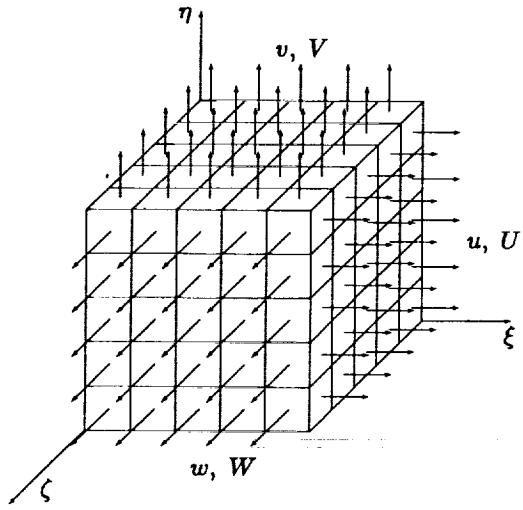

Figure 3. Staggered grid structure in the computational (ξ,η,ζ) space.

The coefficients and source term for the interior points of the discrete $\xi-$momentum equation (29) associated with u_C are given as follows:

$$A_{EE} = -\frac{1}{12Re\Delta\xi^2} + \frac{\eta_{yC}}{12\Delta\xi}(U_{EE} + 2U_{0_{EE}}),$$

$$
\begin{aligned}
A_E &= \frac{4}{3Re\Delta\xi^2} - \frac{2\eta_{yC}}{3\Delta\xi}(U_E + 2U_{0_E}),\\
A_W &= \frac{4}{3Re\Delta\xi^2} + \frac{2\eta_{yC}}{3\Delta\xi}(U_W + 2U_{0_W}),\\
A_{WW} &= -\frac{1}{12Re\Delta\xi^2} - \frac{2\eta_{yC}}{12\Delta\xi}(U_{WW} + 2U_{0_{WW}}),\\
A_{NN} &= -\frac{\alpha_C}{12Re\Delta\eta^2} + \frac{\eta_{yC}}{12\Delta\eta}(V_{nn} + V_{0_{nn}}) - \frac{\gamma_C}{12Re\Delta\eta},\\
A_N &= \frac{4\alpha_C}{3Re\Delta\eta^2} - \frac{2\eta_{yC}}{3\Delta\eta}(V_n + V_{0_n}) + \frac{2\gamma_C}{3Re\Delta\eta},\\
A_S &= \frac{4\alpha_C}{3Re\Delta\eta^2} + \frac{2\eta_{yC}}{3\Delta\eta}(V_s + V_{0_s}) - \frac{2\gamma_C}{3Re\Delta\eta},\\
A_{SS} &= -\frac{\alpha_C}{12Re\Delta\eta^2} - \frac{\eta_{yC}}{12\Delta\eta}(V_{ss} + V_{0_{ss}}) + \frac{\gamma_C}{12Re\Delta\eta},\\
A_{FF} &= -\frac{1}{12Re\Delta\zeta^2} + \frac{\eta_{yC}}{12\Delta\zeta}(W_{ff} + W_{0_{ff}}),\\
A_F &= \frac{4}{3Re\Delta\zeta^2} - \frac{2\eta_{yC}}{3\Delta\zeta}(W_f + W_{0_f}),\\
A_B &= \frac{4}{3Re\Delta\zeta^2} + \frac{2\eta_{yC}}{3\Delta\zeta}(W_b + W_{0_b}),\\
A_{BB} &= -\frac{1}{12Re\Delta\zeta^2} - \frac{\eta_{yC}}{12\Delta\zeta}(W_{bb} + W_{0_{bb}}),\\
A_C &= \frac{3}{2\Delta t} + \frac{5}{2Re}\left(\frac{1}{\Delta\xi^2} + \frac{\alpha_C}{\Delta\eta^2} + \frac{1}{\Delta\zeta^2}\right),\\
D_E &= -D_{WW} = \frac{1}{24\Delta\xi},\\
D_W &= D_C = \frac{27}{24\Delta\xi},\\
S_u &= \frac{-4u_C^n + u_C^{n-1}}{2\Delta t} + \eta_{xC}\frac{-P_{nn} + 8P_n - 8P_s + P_{ss}}{12\Delta\eta} +\\
&\quad \eta_{yC}\left(\frac{-u_{0NN}V_{nn} + 8u_{0N}V_n - 8u_{0S}V_s + u_{0SS}V_{ss}}{12\Delta\eta} +\right.\\
&\quad \left.\frac{-u_{0FF}W_{ff} + 8u_{0F}W_f - 8u_{0B}W_b + u_{0BB}W_{bb}}{12\Delta\zeta}\right) -\\
&\quad \frac{1}{6Re}\left(\eta_{xC}\frac{-u_{\xi nn} + 8u_{\xi n} - 8u_{\xi s} + u_{\xi ss}}{\Delta\eta} + \eta_{zC}\frac{-u_{\zeta nn} + 8u_{\zeta n} - 8u_{\zeta s} + u_{\zeta ss}}{\Delta\eta}\right). \qquad (36)
\end{aligned}
$$

Here, superscripts n and $n-1$ are used to indicate values at previous time steps, and the superscript $n+1$, which indicates the current time step, is dropped for convenience. Lower case subscripts denote the approximate values of the v and w at points where the associated values of u are located (Figure 4). Other symbols used in the above formulas are as follows:

$$
\begin{aligned}
\alpha &= \eta_x^2 + \eta_y^2 + \eta_z^2, \qquad \gamma = \eta_{xx} + \eta_{yy} + \eta_{zz},\\
u_\xi &= \frac{\partial u}{\partial \xi}, \qquad u_\zeta = \frac{\partial u}{\partial \zeta}.
\end{aligned}
$$

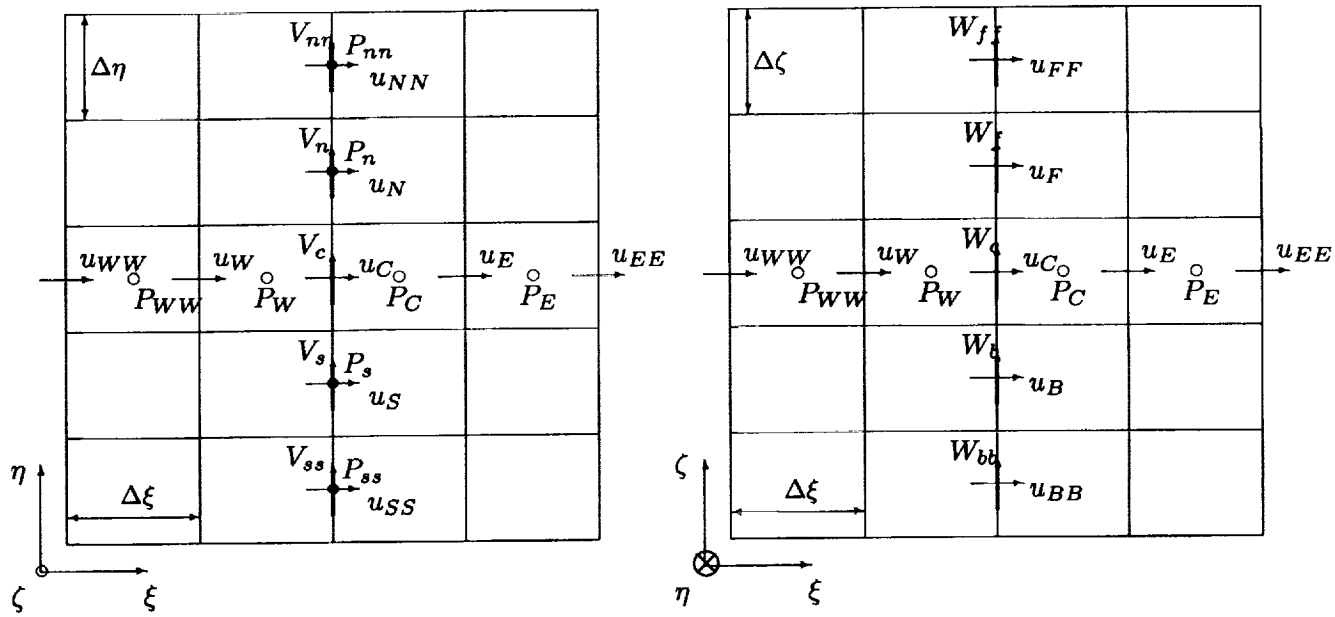

Figure 4. Neighbor points for $\xi-$momentum equation
(U are at the same points as u and are not shown here).

All function values that are required at other than the canonical locations are obtained by fourth-order interpolation in the computational space. For example (see Figure 5),

$$V_c = (9(V_C + v_N + V_{NW} + V_W) - (V_{SWW} + V_{NNWW} + V_{SE} + V_{NNE}))/32, \quad (37)$$

$$P_s = (9(P_S + P_{SW}) - (P_{SE} + P_{SWW}))/16. \quad (38)$$

The coefficients for the $\eta-$ and $\zeta-$ momentum equations are defined in an analogous way, the discrete continuity equation is developed simply by applying central differences to each terms.

On the solid wall boundary points, we change the $\eta-$direction difference to second order, and maintain fourth-order in both the $\xi-$ and $\zeta-$ directions. For more details, see [6].

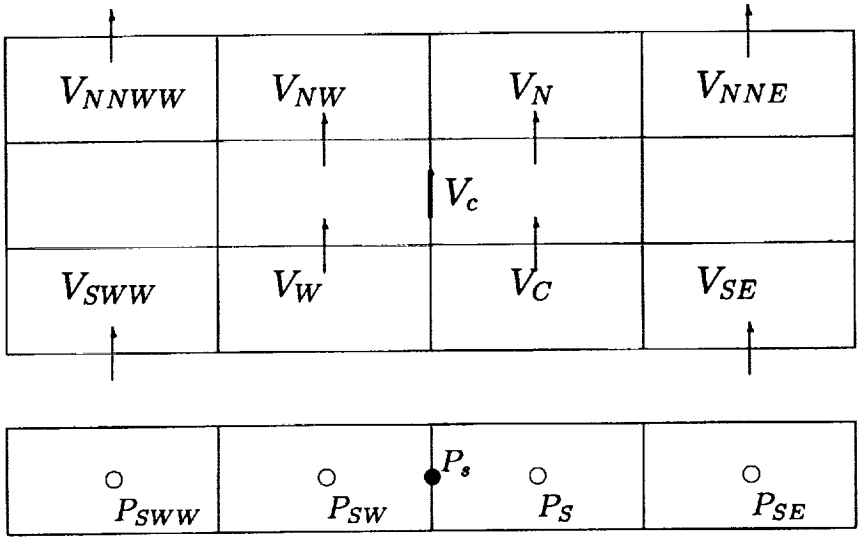

Figure 5. Neighbor points for fourth-order approximation for V_c and P_s.

We use here the same basic line distributive relaxation method developed in our previous work (cf. [5]), with some modifications. Figure 6 shows the distribution of corrections for the group of variables that are located in the (ξ, η) plane.
The process that we use for solving the discrete system (29)–(35) can be described as follows:

- Freezing P, U, V, W, v, and w, perform point Gauss-Seidel relaxation on (29) over the entire computational domain to obtain a new u.
- Freezing P, U, V, W, u, and w, perform point Gauss-Seidel relaxation on (30) over the entire computational domain to obtain a new v.
- Freezing P, U, V, W, u, and v, perform point Gauss-Seidel relaxation on (31) over the entire computational domain to obtain a new w.
- Use transformation (33)–(35) to obtain new U, V, W.
- For all $j = 2, 3, \cdots, n_j - 1$ at once: change $U_{ijk}, U_{i+1\ jk}, V_{ijk}, W_{ijk}, W_{ij\ k+1}$ to satisfy the continuity equations, then update P_{ijk} so that the new U, V, W and P as well as the associated transferred u, v, w satisfy the three momentum equations.

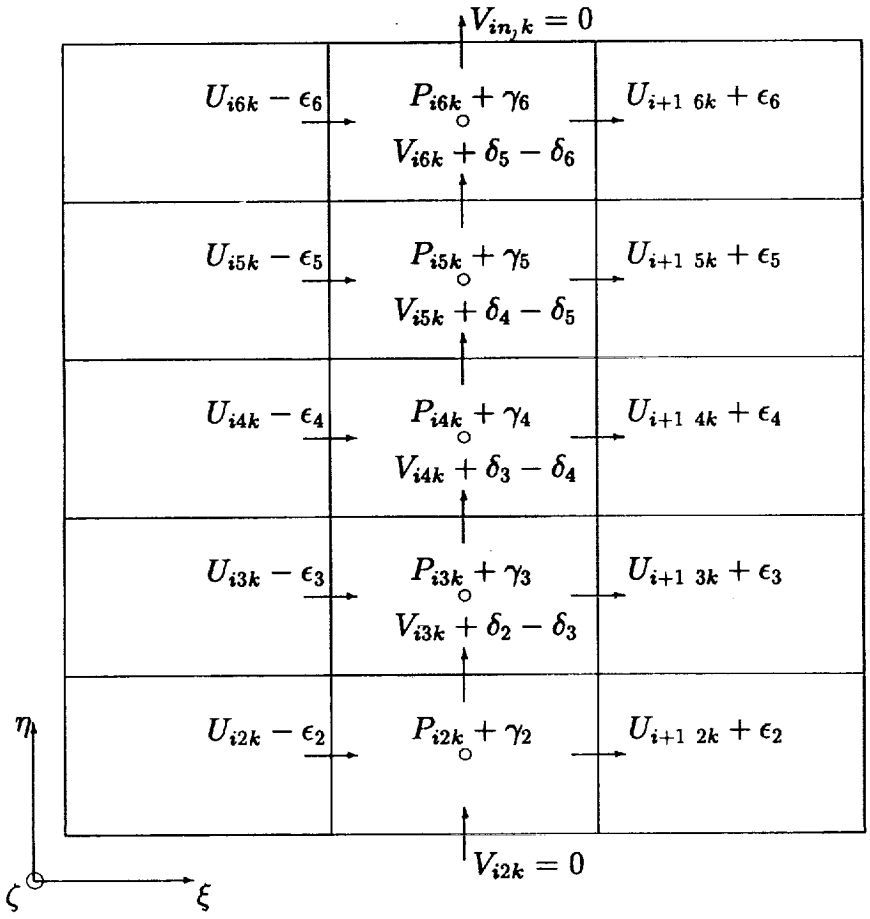

Figure 6. Distribution of corrections in the (ξ, η) plane.

Remark. Since all of the u, v, w have been previously relaxed, and the U, V, W are updated to perform the latter corrections, we assume that equations (29)–(31) hold exactly. Let ϵ, δ, σ and γ represent the corrections for U, V, W and P, respectively. Thus, for cube ijk, when we distribute the corrections according to Figure 6, the correction equations corresponding to (29)–(31) are

$$(A_E^{ijk}\eta_y^{u_{i+1\ jk}} + A_C^{ijk}\eta_y^{u_{ijk}})\epsilon_j - D_C^{ijk}\gamma_j = 0, \quad (39)$$

$$B_N^{ijk}(\delta_j - \delta_{j+1}) - B_C^{ijk}(\delta_{j-1} - \delta_j) - E_C^{ijk}\gamma_j = 0, \quad (40)$$

$$(C_F^{ijk}\eta_y^{w_{ijk+1}} + C_C^{ijk}\eta_y^{w_{ijk}})\sigma_j - F_C^{ijk}\gamma_j = 0, \quad (41)$$

$$(DU_E^{ijk} + DU_C^{ijk})\epsilon_j + (DW_F^{ijk} + DW_C^{ijk})\sigma_j + DV_N^{ijk}(\delta_j - \delta_{j+1}) - DV_C^{ijk}(\delta_{j-1} - \delta_j) = S_m^{ijk}, \quad (42)$$

$$j = 2, 3, \cdots, n_j - 1.$$

This system has $4(n_j - 2)$ equations and $4(n_j - 2)$ variables. Unfortunately, coupling between the correction variables makes the problem somewhat complicated. To develop a simpler approximate system, define

$$\omega_{xj} = \frac{\epsilon_j}{\delta_j},$$

$$\omega_{zj} = \frac{\sigma_j}{\delta_j},$$

with fixed i and k. Then

$$\omega_{xj} = \frac{D_C^{ijk}}{E_C^{ijk}} \frac{(B_N^{ijk} + B_C^{ijk})\delta_j - B_N^{ijk}\delta_{j+1} - B_C^{ijk}\delta_{j-1}}{(A_E^{ijk}\eta_y^{u_{i+1\ jk}} + A_C^{ijk}\eta_y^{u_{ijk}})\delta_j}, \quad (43)$$

$$\omega_{zj} = \frac{F_C^{ijk}}{E_C^{ijk}} \frac{(B_N^{ijk} + B_C^{ijk})\delta_j - B_N^{ijk}\delta_{j+1} - B_C^{ijk}\delta_{j-1}}{(C_F^{ijk}\eta_y^{w_{ijk+1}} + C_C^{ijk}\eta_y^{w_{ijk}})\delta_j}. \quad (44)$$

From (36), we see that $A_C^{ijk} \sim \frac{3}{2\Delta t}$ for high Re and small Δt, which is much larger than A_E^{ijk}. Similarly, $B_C^{ijk} \sim \frac{3}{2\Delta t}$ and $C_C^{ijk} \sim \frac{3}{2\Delta t}$. These yield

$$\omega_{xj} \sim \frac{D_C^j}{E_C^j \eta_y^{u_{ijk}}} = \frac{\Delta\eta}{\Delta\xi \eta_y^{u_{ijk}} \eta_y^{v_{ijk}}}, \quad (45)$$

$$\omega_{zj} \sim \frac{F_C^j}{E_C^j \eta_y^{w_{ijk}}} = \frac{\Delta\eta}{\Delta\zeta \eta_y^{w_{ijk}} \eta_y^{v_{ijk}}}. \quad (46)$$

With the above approximations, ω_{xj} and ω_{zj} can be treated as known parameters, so equation (44) can be written in terms of the unknowns δ_j only:

$$[(DU_E^{ijk} + DU_C^{ijk})\omega_{xj} + (DV_N^{ijk} + DV_C^{ijk}) + (DW_F^{ijk} + DW_C^{ijk})\omega_{zj}]\delta_j - DV_C^{ijk}\delta_{j-1} - DV_N^{ijk}\delta_{j+1} = S_m^{ijk}. \quad (47)$$

Let

$$a_j = (DU_E^{ijk} + DU_C^{ijk})\omega_{xj} + (DV_N^{ijk} + DV_C^{ijk}) + (DW_F^{ijk} + DW_C^{ijk})\omega_{zj}, \quad (48)$$

$$b_j = -DV_N^{ijk}, \quad (49)$$

$$c_j = -DV_C^{ijk}, \quad (50)$$

$$j = 2, 3, \cdots, n_j - 1.$$

Then we obtain the tridiagonal system

$$\begin{bmatrix} a_2 & b_2 & & & & \\ c_3 & a_3 & b_3 & & & \\ & \ddots & \ddots & \ddots & & \\ & & \ddots & \ddots & \ddots & \\ & & & c_{n_j-2} & a_{n_j-2} & b_{n_j-2} \\ & & & & c_{n_j-1} & a_{n_j-1} \end{bmatrix} \begin{bmatrix} \delta_2 \\ \delta_3 \\ \vdots \\ \vdots \\ \delta_{n_j-2} \\ \delta_{n_j-1} \end{bmatrix} = \begin{bmatrix} S_m^{i2k} \\ S_m^{i2k} \\ \vdots \\ \vdots \\ S_m^{in_j-2\ k} \\ S_m^{in_j-1\ k} \end{bmatrix}. \tag{51}$$

Thus, $\delta_j,\ j = 2, 3, \cdots, n_j - 1$ can be determined very efficiently. The other velocity corrections are given by

$$\begin{aligned} \epsilon_j &= \omega_{xj}\delta_j, \qquad \sigma_j = \omega_{zj}\delta_j, \\ & j = 2, 3, \cdots, n_j - 1. \end{aligned}$$

The u, v, and w are then updated on all cells in the i, k $y-$line as follows:

$$\begin{aligned} U^{i+1\ jk} &\leftarrow U^{i+1\ jk} + \epsilon_j, \\ U^{ijk} &\leftarrow U^{ijk} - \epsilon_j, \\ W^{ij\ k+1} &\leftarrow W^{ij\ k+1} + \sigma_j, \\ W^{ijk} &\leftarrow W^{ijk} - \sigma_j, \qquad (52) \\ & j = 2, 3, \cdots, n_j - 1, \\ V^{ijk} &\leftarrow V^{ijk} + \delta_{j-1} - \delta_j, \qquad (53) \\ & j = 3, 4, \cdots, n_j - 1. \end{aligned}$$

Finally, the pressure corrections γ_j are determined as follows:

$$\gamma_2 = \frac{\frac{\Delta\eta}{\Delta\xi}A_C^{i2k} + B_C^{i3k} + \frac{\Delta\eta}{\Delta\zeta}C_C^{i2k}}{(\frac{1}{\Delta\xi} + \frac{1}{\Delta\eta} + \frac{1}{\Delta\zeta})\eta_y^{v_{i3k}}}\delta_j, \tag{54}$$

$$\gamma_j = \frac{\frac{\Delta\eta}{\Delta\xi}A_C^{ijk} + B_C^{ijk} + \frac{\Delta\eta}{\Delta\zeta}C_C^{ijk}}{(\frac{1}{\Delta\xi} + \frac{1}{\Delta\eta} + \frac{1}{\Delta\zeta})\eta_y^{v_{ijk}}}\delta_j, \tag{55}$$

$$j = 3, \cdots, n_j - 1.$$

P is then updated via

$$\begin{aligned} P_{ijk} &\leftarrow P_{ijk} + \gamma_j, \qquad (56) \\ j &= 2, 3, \cdots, n_j - 1. \end{aligned}$$

COMPUTATIONAL RESULTS

We first tested the code by applying it to single and double roughness elements using a moderate sized grid. A $170 \times 50 \times 4$ grid, including a five T-S wavelength physical domain and a one wavelength buffer domain, was used. Considering that $Re = 5000$ corresponds to a decreasing mode according to the linear stability theory, we use this Reynolds number in our code to investigate the effect of roughness elements. Fourier analysis is used to decompose different Fourier modes of the disturbance. For details about the Fourier transformation approach, see [8].

Let $\kappa_l \equiv 0.15$ and $b_l \equiv \sqrt{2}$. For the single roughness case, the peak point is at $i = 30$; for the double roughness case, the peak points are at $i = 42$ and $i = 70$. The stretch parameter σ is set to 4, and the amplitude of the disturbance ϵ is set to $0.0025\sqrt{2}$. Figure 7 displays contours of the perturbation streamfunctions, showing that the roughness elements make the disturbance increase for a certain distance downstream. The results of Fourier transformation given in Figure 8 show that the mean flow distortion and first and second harmonic waves are amplified over this distance.

To test the effect of multiple elements, a $402 \times 66 \times 4$ grid (including a nine wavelength physical domain and a one wavelength buffer domain) is used. Here we set $\kappa_l \equiv 0.12$, $b_l \equiv 2.0$, and $\sigma = 4.5$. The first roughness is at $i = 82$, which is two wavelengths from the inflow boundary. We placed seven roughness elements in the computational domain, starting from $i = 82$ and spared 40 grid points apart. Figures 9 and 10 depict the contour plots of streamfunctions and vorticities, showing very clearly that the disturbance is amplified after it passes each element.

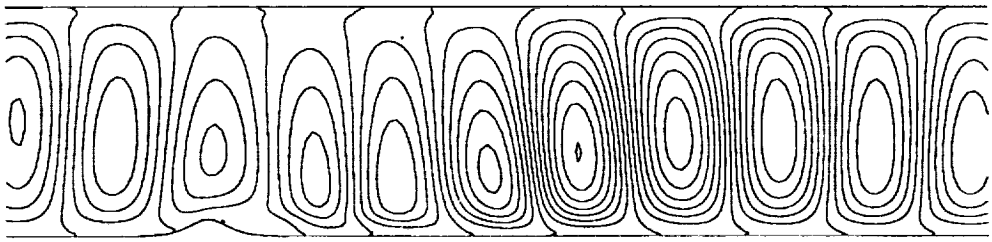

(a)

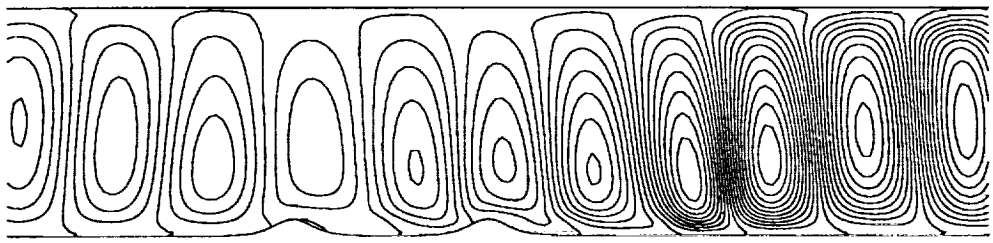

(b)

Figure 7. Contours of perturbation streamfunctions with $Re = 5000$, $\kappa_l = 1.5$, $\epsilon = 0.0025\sqrt{2}$ and $170 \times 50 \times 4$ grid. Flow direction is from left to right.

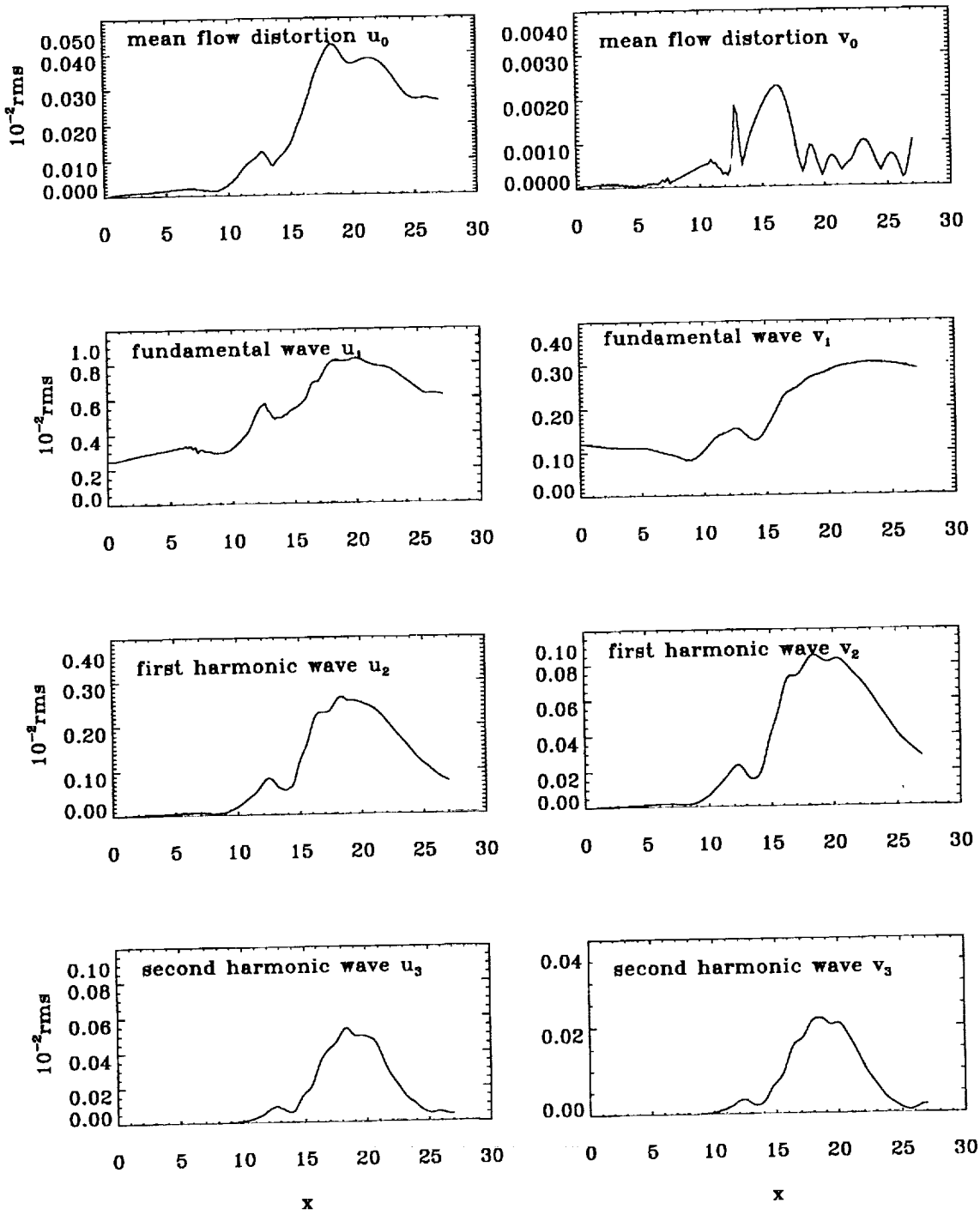

Figure 8. Maximum amplitudes of fundamental wave u_1, v_1, mean-flow distortion u_0, v_0, first harmonic wave u_2, v_2, and second harmonic wave u_3, v_3 for $Re = 5000$, $\kappa_l = 0.15$, and $\epsilon = 0.0025\sqrt{2}$ with two roughness elements (grid: $170 \times 50 \times 4$).

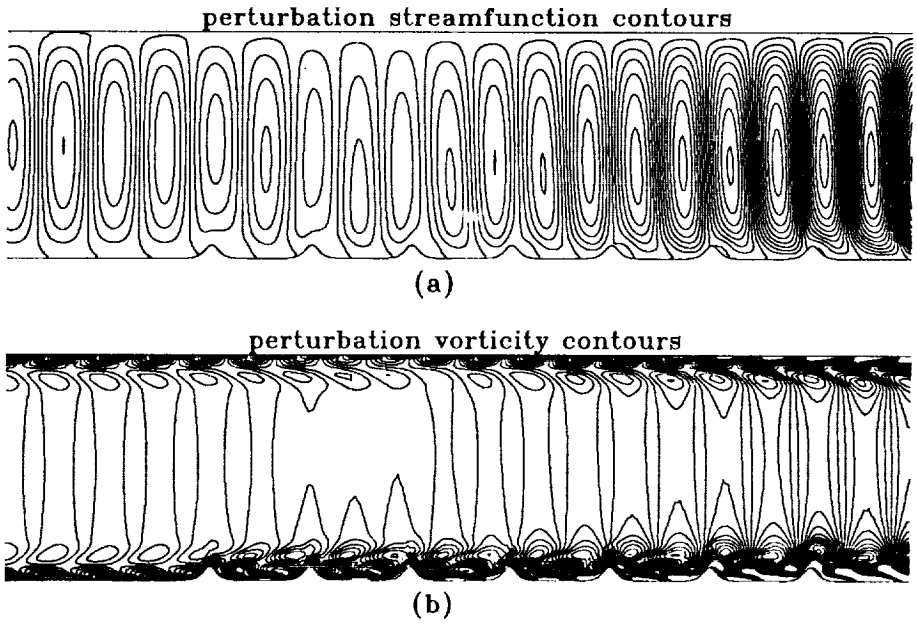

Figure 9. Contour plots of perturbation streamfunctions and vorticities for $Re = 5000$, $\kappa_l = 0.12$, and $\epsilon = 0.0025\sqrt{2}$ with seven roughness elements (grid: $402 \times 66 \times 4$, flow direction is from left to right).

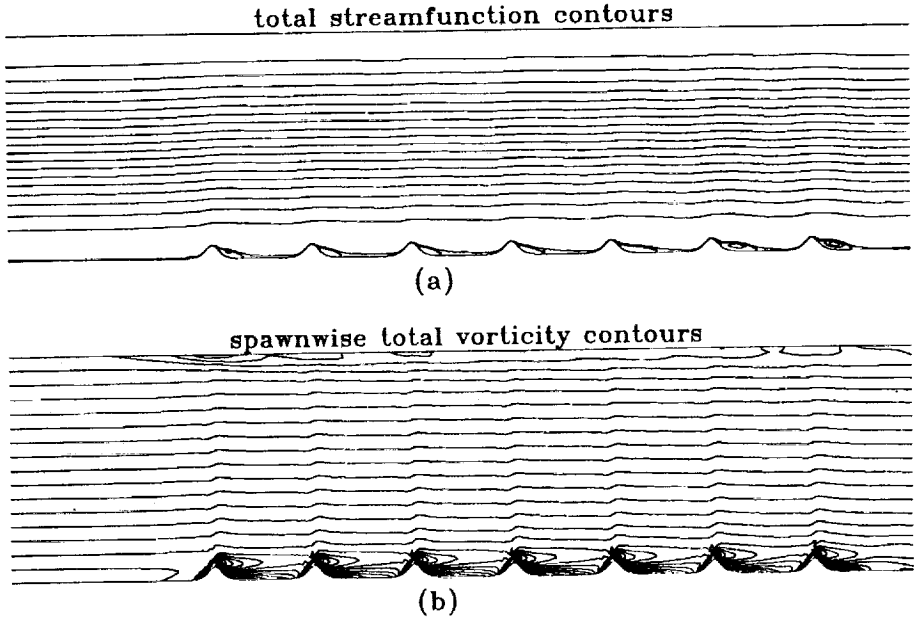

Figure 10. Contour plots of total streamfunctions and vorticities for $Re = 5000$, $\kappa_l = 0.12$, and $\epsilon = 0.0025\sqrt{2}$ with seven roughness elements (grid: $402 \times 66 \times 4$, flow direction is from left to right).

CONCLUDING REMARKS

As expected on physical grounds, we find that the spatial growth rates of the disturbance increase when surface roughness is present. Though our work is limited to roughness without stagnation points in the computational domain, such a scope includes a rather large variety of real roughness elements. Moreover, the code is very efficient, requiring about 2.68 seconds per time step for the $402 \times 66 \times 4$ grid case (equivalent to about 26 μs per time step per grid point).

ACKNOWLEDGEMENT

The authors thank Dr. R. Joslin at NASA Langley Research Center for providing inflow data and general guidance, and Dr. Helen Reed at Arizona State University for sharing her experience.

References

[1] P.S. Klebanoff and K.D. Tidstrom, Mechanism by which a two-dimensional roughness element induces boundary-layer transition, *Phys. Fluids* **15** No.7, 1173–1188 (1972).

[2] G. Danabasoglu, S. Biringen, and C.L. Streett, Spatial simulation of boundary layer instability: effect of surface roughness, *AIAA 93-0075* (1993).

[3] C.Liu, Z.Liu, and S.McCormick, Multigrid methods for flow transition in planar channel, *Comput. Phys. Commun.* **65**, 188-200 (1991).

[4] Z.Liu and C.Liu, Fourth order finite difference and multigrid methods for modeling instabilities in flat plate boundary layers, *J. Comput. Wind. Eng.* **52** 412–417 (1992).

[5] C. Liu and Z. Liu, Multigrid methods for modeling the secondary instabilities in a 3-D channel – temporal and spatial approaches, *Science Report to NASA Langley Research Center,* July 16, 1992.

[6] C.Liu, Z.Liu, and S. McCormick, High order finite difference and multigrid methods for spatially-evolving instability in a planar channel, *J. Comput. Phys.* (in press).

[7] C.L. Streett and M.G. Macaraeg, Spectral multi-domain for large-scale fluid dynamics simulations, *Appl. Num. Math.* **6**, 123–139 (1989).

[8] Z. Liu, C. Liu, and S. McCormick, A comparison with spectral methods and parabolic stability equation theories for transition over a flat plate, *Science Report to NASA Langley Research Center,* October 10, 1992.